



Leveraging machine learning for quantitative precipitation estimation from Fengyun-4 geostationary observations and ground meteorological measurements

5 Xinyan Li¹, Yuanjian Yang¹, Jiaqin Mi¹, Xueyan Bi², You Zhao¹, Zehao Huang¹, Chao Liu¹, Lian Zong¹, and Wanju Li²

1School of Atmospheric Physics, Nanjing University of Information Science and Technology, Nanjing, 210044, China
2Institute of Tropical and Marine Meteorology, China Meteorological Administration, Guangzhou, 510080, China

Correspondence to: Yuanjian Yang (yyj1985@nuist.edu.cn)

10

Abstract Deriving large-scale and high-quality precipitation products from satellite remote sensing spectral data is always challenging in quantitative precipitation estimation (QPE), and limited studies have been conducted even using the China's latest Fengyun-4A (FY-4A) geostationary satellite. Taking three rainstorm events over South China as examples, a Random Forest (RF) model framework for FY-4A QPE during daytime/nighttime is established by using FY-4A multi-band spectral information, cloud parameters, high-density precipitation observations, and physical quantities from reanalysis data. During daytime (nighttime), the probability of detection of the RF model for precipitation is 0.99 (0.99), while the correlation coefficient and root-mean-square error between the retrieved and observed precipitation are 0.77 (0.82) and 1.84 (2.32) mm/h, respectively, indicating that the RF model of FY-4A QPE has high precipitation retrieval accuracy. In particular, the RF model exhibits good spatiotemporal predictive ability for precipitation intensities within the range of 0.5–10 mm/h. For the retrieved accumulated precipitation, the precipitation intensity exhibits a greater impact on the predictive ability of the QPE algorithm than the precipitation duration. Due to the higher density of automatic stations in urban areas, the accuracy of FY-4A QPE over such areas is higher compared with rural areas. Both the accumulated precipitation and the distribution density of automatic stations are more important factors for the predictive ability of the RF model of FY-4A QPE. In general, our proposed FY-4A QPE algorithm has advantages for near-real-time monitoring of summer precipitation over East Asia.

1 Introduction

Precipitation is an important element of weather and climate systems, as well as the global cycling of water and energy (Hobbs, 1989; Fu et al., 2017; Yang et al., 2021). Accurate precipitation observations are important to industrial and



agricultural production, water use, and flood and drought monitoring (Behrangi et al., 2014; Gan et al., 2016; Lolli et al.,
30 2020). Traditional ground-station observations of precipitation possess extremely high measurement accuracy on the point
scale, but they cannot accurately reflect the precipitation on the surface scale owing to the sparse distribution and network
density of stations (Li et al., 2013; Liu et al., 2013). Ground-based radar observations can give the spatial and temporal
distribution of precipitation within a 300-km radius range, but their spatial coverage cannot be scaled up to the global scale
(Lee et al., 2015). With the rapid development of remote sensing, meteorological satellites have become the only viable way
35 to observe precipitation globally at both high spatial and temporal resolution (Tang et al., 2016; Hou et al., 2014). However,
large-scale and high-quality precipitation products derived from satellite remote sensing spectral data have always been a
challenging issue in satellite quantitative precipitation estimation (QPE) (Lensky and Rosenfeld, 1995; Min et al., 2019).
With the constant improvement of meteorological satellites, satellite-based QPE technology has developed greatly. QPE
satellite spectrum precipitation retrieval algorithms can be divided into visible/infrared (VIS/IR), microwave, and multi-
40 combined spectral signals (Kidd, 2010; Levizzani et al., 2007). VIS/IR precipitation retrieval algorithms mainly include the
Geostationary Operational Environmental Satellite (GOES) Precipitation Index algorithm (Arkin and Meisner, 2009), the
GOES Multispectral Precipitation Algorithm (Ba et al., 2001), the Griffith–Woodley algorithm (Griffith et al., 1978), and the
Climate Prediction Center Merged Analysis of Precipitation algorithm (Xie and Arkin, 2001). Microwave precipitation
retrieval algorithms include passive microwave (PMW) precipitation retrieval methods such as the Ferraro algorithm
45 (Ferraro and Ralph, 1997), Goda profile algorithm (Kummerow et al., 2001), and the Passive Microwave Neural Network
Precipitation Retrieval (Sano' et al., 2014), as well as active precipitation retrieval methods based on the Precipitation Radar
(PR) carried onboard the Tropical Precipitation Measuring Mission satellite (Iguchi et al., 2000). Based on the higher
temporal sampling frequency of geostationary satellites, VIS/IR algorithms are suitable for retrieving continuous
precipitation (Kidd, 2010), while PMW algorithms are better for retrieving instantaneous precipitation with higher accuracy
50 (Ebert and Manton, 1996; Bauer et al., 1995), although PR also has the disadvantage of a limited observation range and
uncertain parameters (Iguchi et al., 2009). Therefore, the development of multi-spectral joint precipitation inversion
algorithms can make up for the shortcomings of single-sensor algorithms (Michaelides et al., 2009; Holl et al., 2010). For
example, Rosenfeld and Gutman (1994) explored the relationship between the effective radius of cloud retrieved by NOAA
satellites and precipitation, and proposed that an effective radius greater than 14 μm should be the threshold for precipitation
55 in the cloud. Previous studies have shown that different cloud microphysical parameters are closely related to the ground-
level precipitation intensity, such as the substantially positive correlation between cloud optical thickness/cloud liquid water
content/cloud effective radius and the surface rain rate, while there is basically a negative correlation between the cloud-top
temperature and surface rain rate (Fu and I, 2014; Nauss et al., 2008; Rosenfeld and Gutman, 1994; Rosenfeld et al., 2012;
Yang et al., 2018).
60 Because precipitation is a highly complex process, however, there is a nonlinear relationship between the surface
precipitation intensity and cloud-top optical physical variables, resulting in certain limitations in the precipitation-estimation
equation constructed with statistical methods (Atkinson and Tatnall, 1997). Machine learning is widely used in satellite QPE
(Kühnlein et al., 2014; Min et al., 2019; Chen et al., 2019; Zhang et al., 2019; Sanò et al., 2015), and the Random Forest (RF)



model is a modern machine-learning technique for classification and regression, as well as a combined self-learning
65 technique, which can easily capture the complex nonlinear relationship between observational and meteorological elements
(Breiman, 2001). It has been widely applied to QPE. For instance, (Kühnlein et al., 2014) divided data from the Spinning
Enhanced Visible and Infrared Imager carried onboard the Meteosat Second Generation satellite into day, dusk and
nighttime to establish an RF model and carry out QPE research, the results of which demonstrated a good effect on the
prediction of rain area and convective precipitation. Min et al. (2019) used Himawari-8 real-time multi-band infrared
70 brightness temperature and the Global Precipitation Measurement product to establish a QPE method based on the RF model,
from which it was found that the accuracy of distinguishing the precipitation area reached 0.87 and its average absolute error
and mean square error were 0.51 mm/h and 2.0 mm/h, respectively. Thus, there is strong evidence that the RF model can be
applied effectively in precipitation monitoring and forecasting. The Fengyun-4 satellite (FY-4A), launched in December
2016, is China's second-generation geostationary meteorological satellite, and carried onboard is the Advanced
75 Geostationary Radiation Imager (AGRI) with 14 spectrum detection bands, covering the visible light, shortwave infrared,
midwave infrared, and longwave infrared bands. Thus far, QPE-based research using FY-4A remains limited, especially in
terms of the lack of an RF-based FY-4A QPE framework.

South China is one of the regions in the country with the longest rainy season, the most abundant precipitation, and frequent
heavy rains. Affected by the westerly wind system and the East Asian subtropical monsoon, the period from April to June
80 each year is the first rainy season (or the first flood season) in South China. Therefore, it is important to strengthen the study
of precipitation monitoring methods in the first flood season in South China. In the present work, taking South China (109°–
118°E, 20°–26°N) as the research area, a QPE RF algorithm model for FY-4A is proposed by using the spectral reflectance
observations of FY-4A/AGRI, meteorological environmental physical quantities from the fifth major global reanalysis
produced by the European Centre for Medium-Range Weather Forecasts (ERA5), and a precipitation dataset observed by a
85 high-density automatic station network with hourly resolution. The aims of this study are to further improve the multi-
spectral monitoring level of the FY-4A satellite and provide a scientific basis for improving the disaster prevention and
mitigation capabilities of the FY-4A satellite.

2 Data and methods

2.1 Rainstorm cases

90 Rainstorms occurred frequently during the first flood season in South China in 2019, causing huge losses of life and property.
We selected three rainstorms in South China during 2019 that had a long period of precipitation with a large coverage area,
as follows: Case 1: April 11–12, 2019 (Beijing time; if not specified, Beijing time is used); Case 2: June 12–13, 2019; Case 3:
June 23–24, 2019. For the high-density automatic station precipitation data in the range of 109°–118°E and 20°–26°N, after
filtering and deleting the missing and misdetected data, the number of automatic stations for the three cases was 4263, 4610
95 and 4623, respectively. The distribution of high-density automatic stations throughout the country and in the research area is



shown in Figure 1, and the spatial distributions of precipitation during the three South China rainstorms are shown in Figure 2.

In Case 1, large-scale heavy precipitation mainly occurred in the southern coastal area of Guangdong Province. From north to south, there were three bands of precipitation extremes, and the accumulated precipitation gradually decreased from southwest to northeast. In total, 159 automatic stations recorded precipitation exceeding 100 mm within 48 h, and the maximum precipitation in Jiujiang Town, Foshan City (112.99°E, 22.83°N), on the order of 192 mm, reached rainstorm levels.

In Case 2, there was a belt of accumulated heavy precipitation in the northwest mountainous area, and a large area of heavy precipitation in the northeast of the central urban area. The 48-h automatic station precipitation amounts in these two concentrated heavy precipitation areas both exceeded 100 mm, which meant that the precipitation range and precipitation intensity both met the levels for large-scale heavy precipitation. The precipitation of 492 automatic stations exceeded 100 mm within 48 h, and the maximum precipitation was 318.7 mm in Fogang County, Qingyuan City (113.93°E, 23.91°N).

In Case 3, there were three obvious heavy precipitation areas that met the heavy rain level. The heavy precipitation area on the west side extended from Yulin City to the southeast to the north of Maoming City. The distribution of high-density automatic stations in this area is sparse. A central heavy precipitation area covered Guangzhou and its surrounding urban areas with high population density, where the distribution of automatic stations is extremely dense. On the east side, a strong precipitation center formed in the southwest of Longyan City and connected with Meizhou City to the west. The underlying surface is mountainous, meaning that the distribution of automatic stations in this area is sparse. The precipitation of 644 automatic stations exceeded 100 mm within 48 h, and the maximum precipitation was 239.4 mm in Haizhu District of Guangzhou (113.30°E, 23.10°N).

Among the three cases, Case 1 had a small distribution of heavy precipitation, and the accumulated precipitation was the smallest among the three cases. Case 2 had 29 stations with a 48-h accumulated precipitation exceeding 200 mm, and with more extreme heavy precipitation. Case 3 had the largest number of stations meeting the rainstorm level and had a wide distribution. The types of underlying surface covered by the precipitation were diverse, and the center of the rainstorm was located in the central urban agglomeration and densely populated areas, which meant that the threat to human life and property was high, so Case 3 is more typical and representative to be as a study case with respect to other two cases. This paper therefore takes the heavy rain process of June 23–24 as an example to discuss the QPE method of FY-4A based on the RF model and physical quantities. The prediction and validation results of the RF model for Case 1 and Case 2 are provided in the supporting information.

2.2 Data

The 14 bands of FY-4A/AGRI have different detection purposes and can identify different spectral characteristics of different surfaces, clouds or atmospheres (Table S1 in the supporting information). FY-4A/AGRI has a temporal resolution of 15 min and a spatial resolution of 4 km. It meets the requirements for the spatial and temporal resolution of satellite monitoring of rainstorms. In order to train the RF model, we used the FY-4A/AGRI full disk data with a temporal resolution



130 of 1 h and spatial resolution of $4 \text{ km} \times 4 \text{ km}$ during the study period, which contains 14 bands of radiation brightness temperature and reflectance information. At the same time, the combined channel information was constructed based on the level-1 data.

Due to the indirect link between the surface rain rate and the cloud-top brightness temperature (Boris et al., 2008), the inversion accuracy is limited. To ensure stability of training and forecasting, as well as improve the forecasting accuracy, according to existing research (Kühnlein et al., 2014; Min et al., 2019), four level-2 cloud parameter products [cloud-top temperature (CTT), cloud-top height (CTH), cloud type (CLT), and cloud phase (CLP)] observed in real-time from FY-4A were selected. For each cloud parameter product, the temporal resolution is 1 h and the spatial resolution $4 \text{ km} \times 4 \text{ km}$, which is consistent with the 1-level data. CTT and CTH are the cloud-top temperature and height information of cloud pixels obtained by inversion of AGRI infrared channel data, which can be used to determine the likelihood of cloud growth, extinction, and precipitation. CLT is four different cloud phases generated from AGRI infrared channel data—namely, warm liquid water ($> 0^\circ\text{C}$), supercooled liquid water, mixed, and ice. CLP uses data from multiple infrared channels of AGRI to obtain six different cloud types through a series of spectral and spatial tests: water, supercooled water, mixed, thick ice, thin ice, and multi-layer ice. CLT and CLP are commonly used to detect and track changes in water vapor composition in clouds and extreme weather forecasts to improve extreme weather warning capabilities.

145 In addition to the FY-4A/AGRI observation data, this paper also uses physical quantities from ERA5 to further improve the performance of the QPE algorithm. These data have a horizontal resolution of $0.25^\circ \times 0.25^\circ$, a vertical resolution of 37 layers, and a temporal resolution of up to 1 h. ERA5 is widely used in the study of weather and climate change. According to previous studies (Min et al., 2019; Kanamitsu and Masao, 1989), we introduce some ERA5 reanalysis data to further and better support QPE, including six physical weather indexes, which can effectively describe the atmospheric heat (K-Index), dynamics [convective available potential energy (CAPE); eastward turbulent surface stress (EWSS)], humidity [total column water vapour (TCWV); total column water (TCW)] and topographic features [anisotropy of sub-gridscale orography (ISOR)]. These indexes are closely associated with the initiation and development of clouds that produce rain (Zhang and Guang, 2003; Roman et al., 2016).

2.3 RF model design

155 A data-driven regression model was established between the observed precipitation and satellite spectrum as well as cloud parameters using the RF method. The establishment of the RF model needs to determine two important parameters—namely, the number of input variables of tree nodes, m_{try} , and the number of decision trees, n_{tree} . The essence of the RF data packet estimation is as follows: Randomly create m_{try} pieces of variables for the binary tree on the node, and the choice of the binary tree variables still meets the principle of minimum node impurity. The Bootstrap self-help method is applied to randomly select n_{tree} sample sets from the original dataset to form a decision tree of n_{tree} , and the unsampled samples are used for the prediction of a single decision tree. Samples are classified or predicted according to the RF composed of n_{tree} decision trees. The principle of classification is the voting method, and the principle of prediction is the simple average. Besides, the larger the m_{try} , the smaller the overfitting effect of the RF algorithm; while the larger the n_{tree} , the smaller the



165 difference between the submodels. The value of $mtry$ should be smaller than the value of the input variable. In general, $mtry$
values are 1 , $k/2$, $\sqrt[3]{k}$ and $\log_2(k) + 1$ etc., where k is the number of variables input into the model. We selected $k/2$ as the
number of input variables of the tree node; that is, $mtry = 6$. The number of decision trees, $ntree$, is ideally classified when
the value of $ntree$ is between 500 and 800. We set it to 550.

According to previous studies (Yang et al., 2020; Zeng et al., 2020), a ten-fold cross-validation (10-fold cv) method was
used to test the model estimation performance. The 10-fold cv method makes maximum use of the existing sample data
170 and ensures that each sample is used as a training sample and a test sample respectively, effectively avoiding the result of
over-fitting.

The input variables to the RF model are shown in Table 1, including geographic information, channel information, combined
channel information, cloud parameter products, and ERA5 data. A Daytime Quantitative Precipitation Estimate (DQPE)
algorithm and a Nighttime Quantitative Precipitation Estimate (NQPE) algorithm were constructed separately, due to
175 different input variables between daytime and nighttime. The DQPE algorithm is used to predict the precipitation from 8:00
to 16:00, and the NQPE algorithm is used to predict the remaining time periods. The visible light channel at nighttime cannot
produce valid observational information, so the NQPE algorithm removes these variables. The CTT gradient in the combined
channel information is closely related to the rain rate, defined as follows Eq. (1):

$$\text{Gradient} = \left\{ [T(i+1, j) - T(i-1, j)]^2 + [T(i, j+1) - T(i, j-1)]^2 \right\}^{\frac{1}{2}}, \quad (1)$$

180 where T represents the spectral brightness temperature of $10.7 \mu\text{m}$, and i and j represent the pixel position.

Figure 3 shows the flowchart for the QPE algorithm using the RF model. We selected the 1-h temporal resolution high-
density automatic station geographic and precipitation information, satellite observation data and ERA5 reanalysis data to
input into QPE algorithm for precipitation prediction. The spatial resolution of FY-4A/AGRI is $4 \text{ km} \times 4 \text{ km}$, while that of
ERA5 is $0.25^\circ \times 0.25^\circ$. Due to this difference in spatial resolution, the abovementioned data needed to be interpolated to
185 construct a dataset that was synchronized in time and space. According to previous study (Liu et al., 2020), the differences
between a diverse of interpolation methods are small for high-density automatic stations, with the effect of interpolation
depending mainly on the station distribution rather than the interpolation method itself. In this paper, for matching input
variables with precipitation data, we employed spline interpolation on the satellite data to match the in-situ precipitation
measurement, while used the averaged value of four nearest grids of ERA5 data around each weather station to match the in-
190 situ precipitation measurement/ satellite data at each pixel. The training set was input into the RF model, and the QPE
algorithm with the highest prediction accuracy was constructed by performing 10-fold cv. The testing set was input into the
RF model to obtain the precipitation prediction of each pixel and judge whether the pixel was a precipitation pixel. For a
pixel with a precipitation intensity greater than 0.1 mm/h , it was judged as a precipitation pixel; otherwise, it was judged as a
non-precipitation pixel.

195 Table 2 defines four indicators to judge the accuracy of the QPE algorithm. POD and FAR respectively represent the
probability of detection and false-alarm ratio. The optimal value of POD is 1, and the worst value is 0. On the contrary, the
optimal value of FAR is 1, and the worst value is 0. These two indicators can be used to quantitatively evaluate the



classification results of precipitation and non-precipitation pixels. R and RMSE respectively represent the correlation coefficient and root-mean-square error between the precipitation observation value of the high-density automatic stations and the prediction result of the QPE algorithm. The optimal value of R is 1, and the worst value is 0. Since RMSE represents the mean-square error between two types of data, the smaller the RMSE, the better. These two indicators can be used to quantitatively evaluate the accuracy of precipitation prediction based on the QPE algorithm.

3 Results and discussion

3.1 RF model evaluation

This paper uses 10-fold cv to evaluate the accuracy of precipitation prediction. Figure 4 compares the measured precipitation of the high-density automatic stations in the training set and the testing set with the precipitation prediction of the QPE algorithm in the 10-fold cv of the DQPE algorithm and the NQPE algorithm, in which the color bar represents the occurrence frequency on a log scale with an interval of 0.5 mm/h. In the training set, both the measured precipitation and the predicted precipitation are concentrated within 10 mm/h, which reflects that the precipitation in this interval is accurately predicted. When the precipitation is greater than 20 mm/h, the algorithm tends to underestimate the precipitation. The evaluation indicators (POD, FAR, R and RMSE) of the DQPE algorithm are 1.00, 0.46, 0.97 and 0.83 mm/h, while those of the NQPE algorithm are 1.00, 0.48, 0.97 and 1.04 mm/h, respectively.

In the testing set, when the measured rainfall value of pixels is less than 0.5 mm/h, and the predicted precipitation of a large number of pixel samples is less than 3.0 mm/h, it means that the precipitation intensity is overestimated to a certain extent for drizzle areas and non-precipitation areas. At the same time, there is still a large number of measured and predicted pixel samples with precipitation less than 10 mm/h close to the 1:1 line, reflecting the QPE algorithm's strong ability with respect to the moderate rain level. The evaluation indicators of the DQPE algorithm (POD, FAR, R and RMSE) are 0.99, 0.56, 0.77 and 1.84mm/h, while those of the NQPE algorithm are 0.99, 0.59, 0.82 and 2.32 mm/h, respectively. On the whole, based on the POD and FAR of the two algorithms, the DQPE algorithm has a stronger ability to classify precipitation and non-precipitation pixels, and both algorithms can accurately identify precipitation pixels. However, the two algorithms both produce misjudgments, with a probability of about 50%, for non-precipitation pixels. Based on the R and RMSE of the two algorithms, the NQPE algorithm has a stronger ability to predict precipitation, but it is accompanied by greater uncertainty, possibly because of the increase in the number of heavy rain samples at nighttime.

It can be found that the R of the testing set of the algorithm decreases significantly compared with the training set. The main reasons are as follows: Precipitation is a very complex physical process, although the 10-fold cv method is used to increase the sample size, the number of sample is still small, which leads to the over-utilization of certain sample data, so there is a over-fitting phenomenon. In summary, both the DQPE algorithm and the NQPE algorithm have strong precipitation prediction capabilities, especially for precipitation intensities less than 10 mm/h. When the precipitation intensities more than 10 mm/h, the predicted precipitation is often underestimated for most samples, this is because there are fewer training



230 samples to achieve rainstorm level and above. This kind of prediction error can be reduced by secondary training. The
predictive effect of the QPE algorithm on Case 1 and Case 2 is shown in Figure S1 of the supporting information.

3.2 Application of the RF model to QPE

Figure 5 shows the hourly precipitation distribution as predicted by the DQPE algorithm, and Figure 6 shows the actual
235 precipitation observations at high-density automatic stations in the daytime, with a temporal resolution of 1 h. Comparison of
Figures 5 and 6 shows that the precipitation prediction of the DQPE algorithm is consistent with the actual precipitation
observations at high-density automatic stations, and the DQPE algorithm can capture the precipitation range well. However,
when the precipitation exceeds 20 mm/h, the algorithm obviously underestimates the precipitation. At the same time, the
algorithm tends to overestimate the precipitation when the precipitation is about 0.5 mm/h. This means that the algorithm can
240 only roughly predict the location and range of extreme precipitation pixels, but cannot accurately and quantitatively predict
extreme precipitation. This is similar to the results of previous studies (Kühnlein et al., 2014; Min et al., 2019). At 11:00–
16:00 on June 24, the precipitation center gradually moved to the sea surface. Due to the lack of geographic information
provided by the high-density automatic stations for training at the sea surface, the accuracy of the prediction is low. However,
for land-surface precipitation, the size, location and coverage of the precipitation predicted by the DQPE algorithm is highly
245 consistent with the actual precipitation observations. The algorithm has a good prediction effect and high applicability and
promotional value. The precipitation prediction of Case 1 and Case 2 by the DQPE algorithm is shown in Figure S2 of the
supporting information. The distribution of the measured precipitation in the daytime from the high-density automatic
stations in Case 1 and Case 2 is shown in Figure S3 of the supporting information.

Figure 7 shows the hourly distribution of precipitation as predicted by the NQPE algorithm, and Figure 8 shows the actual
250 precipitation observed at the high-density automatic stations at nighttime. Comparing Figures 7 and 8, a conclusion similar
to that from the DQPE algorithm can be obtained. The precipitation prediction of Case 1 and Case 2 by the NQPE algorithm
is shown in Figure S4 of the supporting information. The distribution of precipitation at nighttime observed by the high-
density automatic stations in Case 1 and Case 2 is shown in Figure S5 of the supporting information. In general, the
prediction ability of the QPE algorithm is strong over the land surface, especially for moderate and light rain with
255 precipitation intensity less than 10 mm/h, with extremely high accuracy. This proves the applicability and feasibility of
establishing an RF model and training the QPE algorithm based on the model variables in Table 1.

3.2 Verification of the QPE results

In order to further analyse the factors that affect the prediction accuracy of the QPE algorithm, we selected three city stations
as research targets: Guangzhou (113.28°E, 23.11°N), Shantou (116.46°E, 23.22°N), and Zhuhai (113.57°E, 22.27°N). At the
260 same time, we selected three rural stations as research targets: Baoshan Mountain (117.94°E, 25.70°N), Lianshan Mountain
(112.09°E, 24.57°N), and Jinxiu (110.11°E, 24.09°N). Figure 9 shows the actual precipitation observations of these six
stations and the accumulated precipitation predicted by the QPE algorithm for 48 consecutive hours.



For the city stations of Guangzhou, Shantou and Zhuhai, the absolute errors of the precipitation prediction are 3.41 mm, 0.40 mm and 3.76 mm, and the relative errors are 2.77%, 0.66% and 33.60%, respectively. For the rural stations of Baoshan, Lianshan and Jinxiu, the absolute errors are 39.15 mm, 8.79 mm and 30.60 mm, and the relative errors are 117.91%, 13.39% and 186.61%, respectively. The prediction error of the city stations is much lower than that of the rural stations, indicating that the QPE algorithm for city stations is more reliable. In the QPE algorithm, geographic information is an important parameter. The distribution of stations in rural areas is less dense than that of the city (Figure 1), meaning that the training provided by the geographic information of the rural stations is insufficient. Therefore, the QPE algorithm has a lower prediction accuracy than the rural stations. The 48-hour accumulated precipitation at Guangzhou Station is 123.2 mm, reaching the rainstorm level, while that at Shantou Station is 60.50 mm, reaching the heavy rain level (Figure 9(a,b)). The precipitation prediction accuracy of the two stations is far better than that of Zhuhai Station, whose 48-hour accumulated precipitation is 14.9 mm in the moderate rain level (Figure 9(c)). The 48-hour accumulated precipitation at Lianshan Station is 65.5 mm, reaching the heavy rain level, the precipitation prediction accuracy of which is far better than that of the other rural stations with accumulated precipitation at the moderate rain level (Figure 9(c, d, f)). This shows that the influence of the rain level on the precipitation prediction accuracy of the QPE algorithm is greater than that of the density of the station distribution. Moreover, Figure 9 reflects the tendency to overestimate weak precipitation (Figure 9(c, d, f)) and underestimate heavy precipitation (Figure 9(a, e)), which is consistent with the conclusions drawn from Figures 5 and 6 and from Figures 7 and 8.

Figure 10(a) presents the 48-h accumulated precipitation predicted by the QPE algorithm. Compared with Figure 2(c), all three heavy precipitation centers are predicted, and the area and intensity in the precipitation prediction and in the actual observations are basically the same. This shows that the algorithm has strong potential in accurately predicting the intensity and range of precipitation. Figures 10(b) and 10(c) respectively represent the actual precipitation frequency observed by the high-density automatic stations and that predicted by the QPE algorithm. The results indicate that the frequency of precipitation in the northeast of the study area is relatively greater, and vice versa in the southwest. The precipitation frequency predicted by the QPE algorithm is generally greater than observed. This is because there are more non-precipitation events for most stations and the algorithm often incorrectly judges non-precipitation areas as weak precipitation stations owing to the FAR of about 0.5, resulting in a positive bias in the precipitation frequency predicted by the QPE algorithm at each station. The spatial distribution of accumulated precipitation in Case 1 and Case 2 is shown in Figure S6 of the supporting information.

Figure 11 shows the spatial distribution of evaluation indicators of the QPE algorithm for all stations. In Figure 11(a), 3817 stations have a POD of 1.00, accounting for 82.57% of all stations; and 4220 stations have a POD of over 0.90, accounting for 91.28% of all stations. In Figure 11(b), the spatial distribution of FAR has a significant negative correlation with accumulated precipitation. FAR is often lower in areas with more accumulated precipitation, such as the three heavy precipitation centers in the precipitation process mentioned above. On the contrary, the FAR is higher in areas with less accumulated precipitation, such as the southwest coastal area. According to the FAR calculation formula (Table 2), this reduces the FAR by reducing the number of precipitation pixels that are not detected by the stations but are detected by the



QPE algorithm. There is a low-FAR zone in the mountainous area in the northwest of the study area, which does not meet the above characteristics. Combined with the results shown in Figures 8(a) to 8(h), we can see that there has been weak precipitation in the area for at least eight consecutive hours. According to the FAR calculation formula (Table 2), this reduces the FAR by increasing the number of precipitation pixels detected by both stations and the QPE algorithm, which also leads to a decrease in POD. Therefore, FAR is negatively correlated with precipitation intensity and duration. When the precipitation intensity is greater and the duration is longer, the FAR of the QPE algorithm is lower and the QPE algorithm's ability to accurately distinguish between precipitation and non-precipitation pixels is stronger.

For Figure 11(c), there are 2577 stations with $R > 0.8$, accounting for 55.74%, and 658 stations with $R < 0.6$, accounting for 14.23%. Comparing Figures 11(b) and 11(c), the stations with lower R have relatively higher FAR. The 48-h accumulated precipitation of these stations is less than 12.5 mm, and the accumulated precipitation is less than 5 h. This basically means that, during this precipitation process, these stations are in atypical stratus cloud or a convective precipitation process, and the precipitation efficiency is extremely low. For non-precipitation areas in a heavy precipitation process, the QPE algorithm tends to judge them as weak precipitation areas, resulting in high FAR and low R in these areas. Although the QPE algorithm tends to overestimate the weak (non-) precipitation area and underestimate the heavy precipitation area, the absolute error for the underestimated heavy precipitation area is much larger than the overestimated weak (non-) precipitation area. Therefore, the spatial distribution of RMSE in Figure 11(d) is highly consistent with the spatial distribution of 48-h accumulated precipitation in Figure 2(c). The stations with an RMSE greater than 1.2 mm/h in Figure 11(d) are basically connected together, and their coverage is basically the same as the area covered by the stations with a 48-h accumulated precipitation exceeding 50 mm/h in Figure 2(c).

In summary, the predictive ability of the QPE algorithm is as follows: (1) For convective precipitation or stratus convective mixed precipitation with long duration, high intensity and high efficiency, such as in Guangzhou and nearby urban areas in Case 3, the algorithm has a very high POD, low FAR, and R is close to 1. Its RMSE is affected by the precipitation intensity. In this precipitation process, the QPE algorithm has the strongest predictive ability. (2) For precipitation with long duration and weak intensity per unit time, such as the northwest mountainous area in Case 3, the FAR of the QPE algorithm is equivalent to that of the previous type of precipitation. The POD declines slightly, but still exceeds 0.85, and the R also decline slightly, but is still near 0.8. The RMSE is greatly reduced. The predictive ability of the QPE algorithm is second to the previous precipitation process. (3) When the duration of precipitation is short and the intensity is only light to moderate rain, such as in the southwest coastal area in Case 3, the FAR predicted by the QPE algorithm is relatively high, the R is relatively low, and the reliability of the predictive ability of the QPE algorithm is low. For Case 1 and Case 2, the hourly spatial distribution of evaluation indicators for both QPE algorithms at each station is shown in Figure S7 of the supporting information.

Figure 12 shows the time series of evaluation indicators of the QPE algorithm for all stations at each time. The red lines represent the average values of the evaluation indicators, from which we can see that the average values of POD, FAR, R and RMSE are 0.98, 0.60, 0.69 and 1.93 mm/h, respectively. From 01:00 to 14:00 on June 24, the POD, R and RMSE are high and the FAR is low. According to Figures 6(j) to 6(p) and Figures 8(q) to 8(w), the intensity of the precipitation center



during this period exceeds 16 mm/h, reaching rainstorm level. At this point, the prediction accuracy of the QPE algorithm is strong. Not only is the effect of the evaluation indicator good, but also the intensity of the precipitation center and the precipitation range of these periods fit with high accuracy, as can be seen by comparing Figure 5 with Figure 6(j–l) and Figure 7 with Figure 8(q–w). This proves that, for the strong convective process with a short precipitation duration and the precipitation intensity reaching rainstorm level, the evaluation indicators show similar characteristics to the first type of precipitation above. At the same time, this means that when the precipitation intensity is large enough, the precipitation duration is no longer the main factor influencing the predictive ability of the QPE algorithm. At 00:00–04:00 on June 23, the POD, R and RMSE are higher than their average values, while the FAR is lower than its average value. The characteristics of each evaluation indicator during this period are similar to the second type of precipitation above. Comparing Figure 7 with Figure 8(a–d), the precipitation intensity and range are basically successfully fitted, but the prediction of precipitation in localized areas is not good. This verifies the previous conclusion that the QPE algorithm’s predictive ability for long-duration and weak-intensity precipitation is inferior to that of strong convective precipitation. From 17:00 to 20:00 on June 23, the POD, R and RMSE are all lower than their average values, while FAR is higher than its average value. According to Figures 8(i) to 8(l), the precipitation duration during this period is short, the precipitation intensity is weak, and the precipitation process and characteristics are similar to the third type of precipitation above. For Case 1 and Case 2, the time series of evaluation indicators of the QPE algorithm for all stations at each time are shown in Figure S8 of the supporting information.

350 4 Conclusions

By using FY-4A/AGRI spectral observation data, cloud parameter products and physical quantities, a QPE RF model framework for FY-4A was established. The main conclusions are as follows:
Both the DQPE and NQPE RF algorithms for FY-4A have high precipitation prediction accuracy. In detail, the evaluation indicators of POD, FAR, R and RMSE for the DQPE algorithm are 0.99, 0.56, 0.77 and 1.84 mm/h, respectively, while those for the NQPE algorithm are 0.99, 0.59, 0.82 and 2.32 mm/h, respectively. Comparatively, the DQPE algorithm has a stronger ability to classify precipitation and non-precipitation pixels, and the NQPE algorithm has a stronger ability to predict precipitation. The two algorithms have a strong ability to predict the precipitation process when the precipitation is 0.5–10 mm/h. In addition, both algorithms overestimate the precipitation intensity in weak (non-) precipitation areas of 0–0.5 mm/h and underestimate the precipitation intensity in heavy precipitation areas of > 10 mm/h.
The density of the distribution and accumulated precipitation of high-density automatic stations are both important factors affecting the predictive ability of the QPE algorithm. The denser the distribution of high-density automatic stations, with more geographic information provided for model training, the stronger the predictive ability of the QPE algorithm. The stations in South China are densely distributed and provide a lot of geographic information for model training. Therefore, the QPE algorithm constructed in this paper can better capture the distribution range of land-surface precipitation and the center location of strong precipitation. However, due to the lack of high-density automatic stations over the ocean, the QPE



algorithm cannot accurately predict ocean-surface precipitation. Automatic stations are more densely distributed over urban areas than rural areas, resulting in a stronger ability of the QPE algorithm to predict precipitation over urban areas. The QPE algorithm can accurately estimate the trend of change in precipitation and the accumulated amount of precipitation in locations where heavy rain appears, exhibiting small prediction errors. In contrast, the prediction errors of the QPE algorithm become relatively larger when the accumulated precipitation is at the medium to light rain level. Generally, the accumulated precipitation level has a greater impact on the predictive ability of the QPE algorithm than the density of the distribution of automatic stations.

The prediction accuracy of the QPE algorithm for accumulated precipitation is mainly affected by the rain rate, precipitation duration, and precipitation efficiency. More specifically: (1) For strong precipitation processes both long and short in duration and with a high rain rate, the QPE algorithm exhibits its strongest predictive ability, with extremely high POD and R and low FAR. The RMSE is mainly affected by the rain rate. This implies that when the rain rate is large enough, the precipitation duration is no longer affecting the accuracy of the QPE algorithm. (2) For precipitation processes in long duration and with a low rain rate, the POD declines slightly but still exceeds 0.85, the R declines slightly but is still near 0.8, and the RMSE is greatly reduced. (3) When the precipitation duration is short and the intensity is only small to moderate, the FAR of the QPE algorithm is relatively high and the R is relatively low, exhibiting low reliability of the QPE algorithm to predict the precipitation.

In general, by combining high-density automatic station data and meteorological physical quantity fields, the FY-4A QPE algorithm established in the present work offers important scientific support and application value for the real-time monitoring and prediction of summer precipitation over East Asia, as well as rainstorm disaster prevention and reduction. Previous studies have tended only to include cloud-top information; whereas, in contrast, our findings show that it is helpful to improve the ability of inverting precipitation based on satellite cloud parameters through the introduction of meteorological physical variables. Especially, for practical applications in the future, the meteorological physical quantity forecast fields of the global forecast system from China T639, ECMWF or GFS can be combined with real-time FY-4A satellite spectral information and high-density automatic station precipitation information to quantitatively estimate real-time, large-scale, and dynamic continuous precipitation over East Asia by using the RF model framework, which has important implications and broad application value for precipitation monitoring.

Code availability

The model in this paper is based on the random Forest data package in the R language, and our implementation and analysis code are available upon request to the corresponding author (yyj1985@nuist.edu.cn).



395 **Data availability**

All Fengyun-4 satellite data used in this paper can be downloaded from China National Meteorological Satellite Center at <http://www.nsmc.org.cn/NSMC/Home/Index.html>, ERA5 reanalysis data from the Copernicus Climate Change Service at <https://cds.climate.copernicus.eu/cdsapp#!/dataset/reanalysis-era5-single-levels?tab=form>. The data of high-density automatic stations are not available to the public. Please direct any inquiries regarding the data to the corresponding author

400 (yyj1985@nuist.edu.cn).

Supplement

The supplement related to this paper is available online at: [Supplement](#).

Author contributions

Conceptualization, Y.Y.; methodology, X.L. and Y.Y.; software, X.L.; validation, G.N. and Y.Y.; formal analysis, X.L., and
405 Y.Y.; data curation, X.L., Z.L., and W.L.; writing—original draft preparation, X.L.; writing—review and editing, X.B., Y.Z.,
Z.H., C.L., and Y.Y.; visualization, X.L. and J.M.; supervision, Y.Y.; funding acquisition, Y.Y. All authors have read and
agreed to the published version of the manuscript.

Competing interests

The authors declare that they have no conflict of interest.

410 **Acknowledgements**

The author would like to thank Yali Chao of Sun Yat-sen University helped in drawing the distribution map of high-density automatic stations.

Financial support

This research has been supported by the National Key Research and Development Program of China (grant
415 no.2018YFC1506502), the National Natural Science Foundation of China (grant no. 42061134009), University Student
Innovation Training Project of Jiangsu China (grant no. 202010300057Y).

References

Arkin, P. A. and Meisner, B. N.: The Relationship between Large-Scale Convective Rainfall and Cold Cloud over the



- Western Hemisphere during 1982-84, *Mon. wea. rev.*, 115, doi: 10.1175/1520-0493(1987)115<0051:TRBLSC>2.0.CO;2,
420 2009.
- Atkinson, P. M. and Tatnall, A. R. L.: Introduction Neural networks in remote sensing, *International Journal of Remote Sensing*, 18, 699-709, doi: 10.1080/014311697218700, 1997.
- Ba, Mamoudou, B., Gruber, and Arnold: GOES Multispectral Rainfall Algorithm (GMSRA), *Journal of Applied Meteorology*, doi: 10.1175/1520-0450(2001)040<1500:GMRAG>2.0.CO;2, 2001.
- 425 Bauer, P., Schanz, L., Bennartz, R., and Schlüssel, P.: Outlook for combined TMI-VIRS algorithms for TRMM: Lessons from the PIP and AIP projects, *Journal of the Atmospheric Sciences*, 55, 1714-1729, doi: 10.1175/1520-0469(1998)055<1714:OFCTVA>2.0.CO;2, 1995.
- Boris, Thies, Thomas, Nau, Jrg, and Bendix: Precipitation process and rainfall intensity differentiation using Meteosat Second Generation Spinning Enhanced Visible and Infrared Imager data, *Journal of Geophysical Research*, 113, doi:
430 10.1029/2008JD010464, 2008.
- Breiman: Random forests, *MACH LEARN*, 2001,45(1), 5-32, <https://doi.org/10.1023/a:1010933404324>, 2001.
- Chen, H., Chandrasekar, V., Cifelli, R., and Xie, P.: A Machine Learning System for Precipitation Estimation Using Satellite and Ground Radar Network Observations, *IEEE Transactions on Geoscience and Remote Sensing*, PP, 1-13, doi: 10.1109/TGRS.2019.2942280, 2019.
- 435 Ebert, E. E. and Manton, M. J.: Performance of Satellite Rainfall Estimation Algorithms during TOGA COARE, *Journal of the Atmospheric Sciences*, 55, 1537-1557, doi: 10.1175/1520-0469(1998)055<1537:POSREA>2.0.CO;2, 1996.
- Ferraro and Ralph, R.: Special sensor microwave imager derived global rainfall estimates for climatological applications, *Journal of Geophysical Research Atmospheres*, 102, 16715-16735, doi: 10.1029/97JD01210, 1997.
- Fu Y.: Cloud Parameters Retrieved by the Bispectral Reflectance Algorithm and Associated Applications, *Journal of*
440 *Meteorological Research*, 28, 965-982, doi: 10.1007/s13351-014-3292-3, 2014.
- Fu, Y., Pan, X., Yang, Y., Chen, F., and Liu, P.: Climatological characteristics of summer precipitation over East Asia measured by TRMM PR: A review, *Journal of Meteorological Research*, 31, 142-159, doi: 10.1007/s13351-017-6156-9, 2017.
- Gan, T. Y., Ito, M., Hülsmann, S., Qin, X., Lu, X. X., Liang, S.-Y., Rutschman, P., Disse, M., and Koivusalo, H.: Possible
445 climate change/variability and human impacts, vulnerability of drought-prone regions, water resources and capacity building for Africa, *Hydrological Sciences Journal*, 61, 1209-1226, doi: 10.1080/02626667.2015.1057143, 2016.
- Griffith, C. G., Woodley, W. L., Grube, P. G., Martin, D. W., and Sikdar, D. N.: Rain Estimation from Geosynchronous Satellite Imagery—Visible and Infrared Studies, *Monthly Weather Review*, 106, 1153, doi: 10.1175/1520-0493(1978)106<1153:REFGSI>2.0.CO;2, 1978.
- 450 Hobbs, P. V.: Research on Clouds and Precipitation: Past, Present, and Future, Part I, *Bulletin of the American Meteorological Society*, 70, 282-285, doi: 10.1175/1520-0477-70.3.282, 1989.
- Holl, G., Buehler, S. A., Rydberg, B., and Jiménez, C.: Collocating satellite-based radar and radiometer measurements – methodology and usage examples, *Atmospheric Measurement Techniques*, 3, 5826, doi: 10.5194/amt-3-693-2010, 2010.



- Hou, A. Y., Kakar, R. K., Neeck, S., Azarbarzin, A. A., Kummerow, C. D., Kojima, M., Oki, R., Nakamura, K., and Iguchi, T.: The global precipitation measurement mission, *Bulletin of the American Meteorological Society*, 95, 701-722, doi: 10.1175/BAMS-D-13-00164.1, 2014.
- 455 Iguchi, T., Kozu, T., Meneghini, R., and Okamoto, K.: Rain Profiling Algorithm for the TRMM Precipitation Radar, *J.appl.meteor*, 39, doi: 10.2151/jmsj.87A.1, 2000.
- Iguchi, T., Kozu, T., Kwiatkowski, J., Meneghini, R., Awaka, J., and Okamoto, K. I.: Uncertainties in the Rain Profiling Algorithm for the TRMM Precipitation Radar, *Journal of the Meteorological Society of Japan.ser.ii*, 87, 1-30, doi: 10.2151/jmsj.87A.1, 2009.
- 460 Kanamitsu and Masao: Description of the NMC Global Data Assimilation and Forecast System, *Weather & Forecasting*, 4, 335-342, doi: 10.1175/1520-0434(1989)004<0335:DOTNGD>2.0.CO;2, 1989.
- Kidd, C.: Satellite rainfall climatology: a review, *International Journal of Climatology*, 21, doi: 10.1002/joc.635, 2010.
- 465 Kühnlein, M., Appelhans, T., Thies, B., and Naus, T.: Precipitation Estimates from MSG SEVIRI Daytime, Nighttime, and Twilight Data with Random Forests, *Journal of Applied Meteorology and Climatology*, 53, 2457-2480, doi: 10.1175/JAMC-D-14-0082.1, 2014.
- Kummerow, C., Hong, Y., Olson, W. S., Yang, S., Adler, R. F., M Cc Ollum, J., Ferraro, R., Petty, G., Shin, D. B., and Wilheit, T. T.: The Evolution of the Goddard Profiling Algorithm (GPROF) for Rainfall Estimation from Passive Microwave Sensors, *J.appl.meteor*, 40, 1801-1820, doi: 10.1175/1520-0450(2001)040<1801:TEOTGP>2.0.CO;2, 2001.
- 470 Lee, Y. R., Shin, D. B., Kim, J. H., and Park, H. S.: Precipitation estimation over radar gap areas based on geostationary satellite and adjacent radar observations, *Atmospheric Measurement Techniques*, 8, 719-728, doi: 10.5194/amt-8-719-2015, 2015.
- Lensky, I. M. and Rosenfeld, D.: Estimation of Precipitation Area and Rain Intensity Based on the Microphysical Properties Retrieved from NOAA AVHRR Data, *Journal of Applied Meteorology & Climatology*, 36, 234-242, doi: 10.1175/1520-0450(1997)036<0234:EOPAAR>2.0.CO;2, 1995.
- 475 Levizzani, V., Bauer, P., and Turk, F. J.: Measuring Precipitation from Space, *Measuring Precipitation from Space*, doi: 10.1007/978-1-4020-5835-6, 2007.
- Li, Z., Yang, D., and Hong, Y.: Multi-scale evaluation of high-resolution multi-sensor blended global precipitation products over the Yangtze River, *Journal of Hydrology*, 500, doi: 10.1016/j.jhydrol.2013.07.023, 2013.
- 480 Liu, D., Zhao, Q., Fu, D., Guo, S., and Zeng, Y.: Comparison of spatial interpolation methods for the estimation of precipitation patterns at different time scales to improve the accuracy of discharge simulations, *Hydrology Research*, 51, doi: 10.2166/nh.2020.146, 2020.
- Liu, X. C., Gao, T. C., and Liu, L.: A comparison of rainfall measurements from multiple instruments, *Atmospheric Measurement Techniques*, 6, doi: 10.5194/amt-6-1585-2013, 2013.
- 485 Lolli, S., Vivone, G., Lewis, J. R., Sicard, M., Welton, E. J., Campbell, J. R., Comerón, A., D'Adderio, L. P., Tokay, A., and Giunta, A.: Overview of the New Version 3 NASA Micro-Pulse Lidar Network (MPLNET) Automatic Precipitation Detection Algorithm, *Remote Sensing*, 12, 71, doi: 10.3390/rs12010071, 2020.



- Michaelides, S., Levizzani, V., Anagnostou, E., Bauer, P., Kasparis, T., and Lane, J. E.: Precipitation: Measurement, remote
490 sensing, climatology and modeling, *Atmospheric Research*, 94, 512-533, doi: 10.1016/j.atmosres.2009.08.017, 2009.
- Min, M., Bai, C., Guo, J., Sun, F., Liu, C., Wang, F., Xu, H., Tang, S., Li, B., and Di, D.: Estimating Summertime
Precipitation from Himawari-8 and Global Forecast System Based on Machine Learning, *IEEE Transactions on Geoscience
and Remote Sensing*, PP, 1-14, doi: 10.1109/TGRS.2018.2874950, 2019.
- Nauss, T., Thies, B., Turek, A., Bendix, J., and Kokhanovsky, A.: Operational discrimination of raining from non-raining
495 clouds in mid-latitudes using multispectral satellite data, *Precipitation: Advances in Measurement, Estimation and Prediction*,
doi: 10.1007/978-3-540-77655-0_7, 2008.
- Roman, J., Knuteson, R., Ackerman, S., and Revercomb, H.: Estimating Minimum Detection Times for Satellite Remote
Sensing of Trends in Mean and Extreme Precipitable Water Vapor, *Journal of Climate*, 29, doi: 10.1175/JCLI-D-16-0303.1,
2016.
- 500 Rosenfeld, D. and Gutman, G.: Retrieving microphysical properties near the tops of potential rain clouds by multispectral
analysis of AVHRR data, *Atmospheric Research*, 34, 259-283, doi: 10.1016/0169-8095(94)90096-5, 1994.
- Rosenfeld, D., Wang, H., and Rasch, P. J.: The roles of cloud drop effective radius and LWP in determining rain properties
in marine stratocumulus, *Geophysical Research Letters*, 39, doi: 10.1029/2012GL052028, 2012.
- Sano', P., Casella, D., Panegrossi, G., Marra, A. C., and Dietrich, S.: The Passive Microwave Neural Network Precipitation
505 Retrieval (PNPR) for AMSU/MHS and ATMS cross-track scanning radiometers, *Atmospheric Measurement Techniques*, 8,
857, doi: 10.5194/amt-9-5441-2016, 2014.
- Sanò, P., Panegrossi, G., Casella, D., Paola, F. D., Milani, L., Mugnai, A., Petracca, M., and Dietrich, S.: The Passive
microwave Neural network Precipitation Retrieval (PNPR) algorithm for AMSU/MHS observations: description and
application to European case studies, *Atmospheric Measurement Techniques*, doi: 10.5194/amt-8-837-2015, 2015.
- 510 Tang, G., Ma, Y., Long, D., Zhong, L., and Hong, Y.: Evaluation of GPM Day-1 IMERG and TMPA Version-7 legacy
products over Mainland China at multiple spatiotemporal scales, *Journal of Hydrology*, 533, doi:
10.1016/j.jhydrol.2015.12.008, 2016.
- Xie, P. and Arkin, P. A.: Global precipitation: A 17-year monthly analysis based on gauge observations, *Bull. Amer. Meteor.
Soc.*, doi: 10.1175/1520-0477(1997)078<2539:GPAYMA>2.0.CO;2, 2001.
- 515 Yang, Y., Zhang, M., Li, Q., Chen, B., and Luo, M.: Modulations of surface thermal environment and agricultural activity on
intraseasonal variations of summer diurnal temperature range in the Yangtze River Delta of China, *Science of The Total
Environment*, 736, 139445, doi: 10.1007/s00024-018-1940-8, 2020.
- Yang, Y., Wang, R., Chen, F., Liu, C., Bi, X., and Huang, M.: Synoptic weather patterns modulate the frequency, type and
vertical structure of summer precipitation over Eastern China: A perspective from GPM observations, *Atmospheric Research*,
520 249, 105342, doi: 10.1016/j.atmosres.2020.105342, 2021.
- Yang, Y. J., Wang, H., Chen, F., Zheng, X., and Zhou, S.: TRMM-Based Optical and Microphysical Features of
Precipitating Clouds in Summer Over the Yangtze–Huaihe River Valley, China, *Pure and Applied Geophysics*, 176, doi:
10.1007/s00024-018-1940-8, 2018.



- Zeng, Z., Wang, Z., Gui, K., Yan, X., Gao, M., Luo, M., Geng, H., Liao, T., Li, X., and An, J.: Daily Global Solar Radiation
525 in China Estimated From High-Density Meteorological Observations: A Random Forest Model Framework, *Earth and Space
Science*, 7, doi: 10.1029/2019EA001058, 2020.
- Zhang and Guang, J.: Roles of tropospheric and boundary layer forcing in the diurnal cycle of convection in the U.S.
southern great plains, *Geophysical Research Letters*, 30, 2281, doi: 10.1029/2003GL018554, 2003.
- Zhang, C., Yang, X., and Zhang, W.: Accurate Precipitation Nowcasting with Meteorological Big Data: Machine Learning
530 Method and Application, *Journal of Agricultural Big Data*, doi: 10.19788/j.issn.2096-6369.190108, 2019.

535

540

545

550

555



560

Table 1: Variables used in the QPE algorithm.

Variables	
Geographic information	Longitude, Latitude
Channel information of AGRI	T0.47*, T0.65*, T0.825*, T1.375*, T1.61*, T2.25*, T3.75H, T3.75L, T6.25, T7.1, T8.5, T10.7, T12.0, T13.5
Combined information of AGRI	T6.25–T10.7, T8.5–T10.7, T7.1–T12.0, T12.0–T10.7, T3.75L–T7.1, T3.75L–T10.7, Gradient
Cloud parameters of AGRI	CTT, CTH, CLT, CLP
ERA5	ISOR, CAPE, EWSS, K-Index, TCW, TCWV

Notation: asterisk (*) indicates that the variable does not appear in the NQPE algorithm.

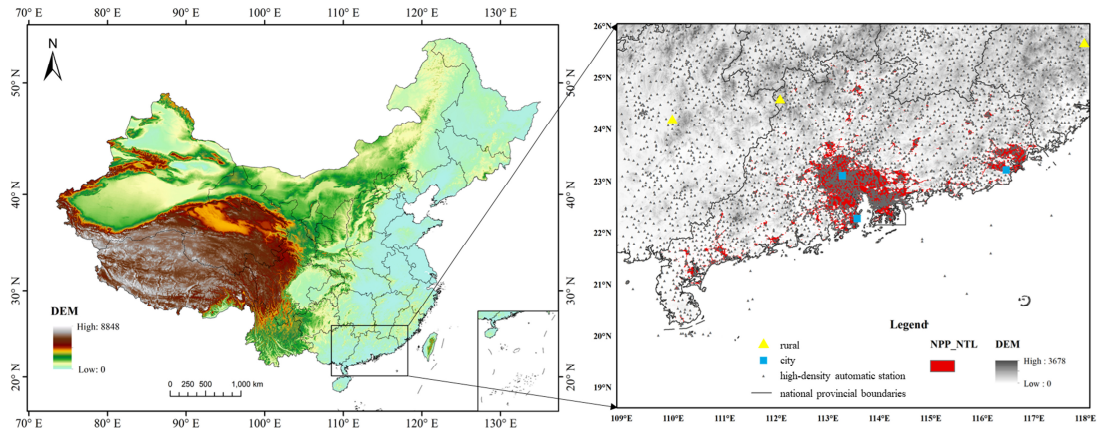


565

Table 2: Evaluation metrics used in this study.

Evaluation metric	Equation
<i>POD</i>	$POD = \frac{A}{A + B}$
<i>FAR</i>	$FAR = \frac{C}{A + C}$
<i>R</i>	$R = \frac{\sum_{i=1}^n (G_i - \bar{G})(S_i - \bar{S})}{\sum_{i=1}^n (G_i - \bar{G}) \sum_{i=1}^n (S_i - \bar{S})}$
<i>RMSE</i>	$RMSE = \sqrt{\frac{1}{n} \sum_{i=1}^n (G_i - S_i)^2}$

Notation: *A* represents the precipitation events detected by both stations and the QPE algorithm; *B* represents the precipitation events detected by the stations but not by the QPE algorithm; *C* represents the precipitation events not detected by the stations but detected by the QPE algorithm; G_i is the precipitation observed by stations; S_i represents the precipitation predicted by the QPE algorithm.



570 **Figure 1: Distribution of high-density automatic stations throughout the country and in the research area.**

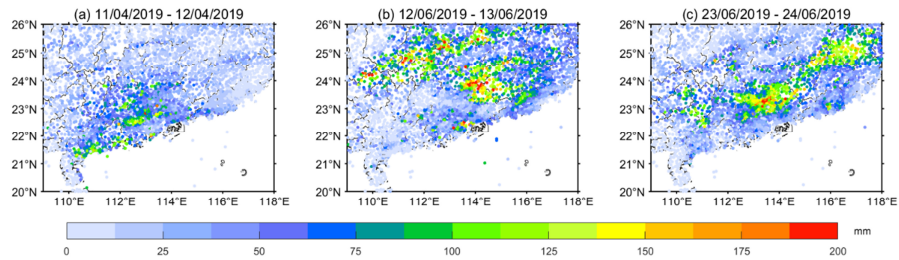


Figure 2: Spatial distribution of precipitation during the three South China rainstorms: (a) April 11-12, 2019; (b) June 12-13, 2019; (c) June 23-24, 2019.



575

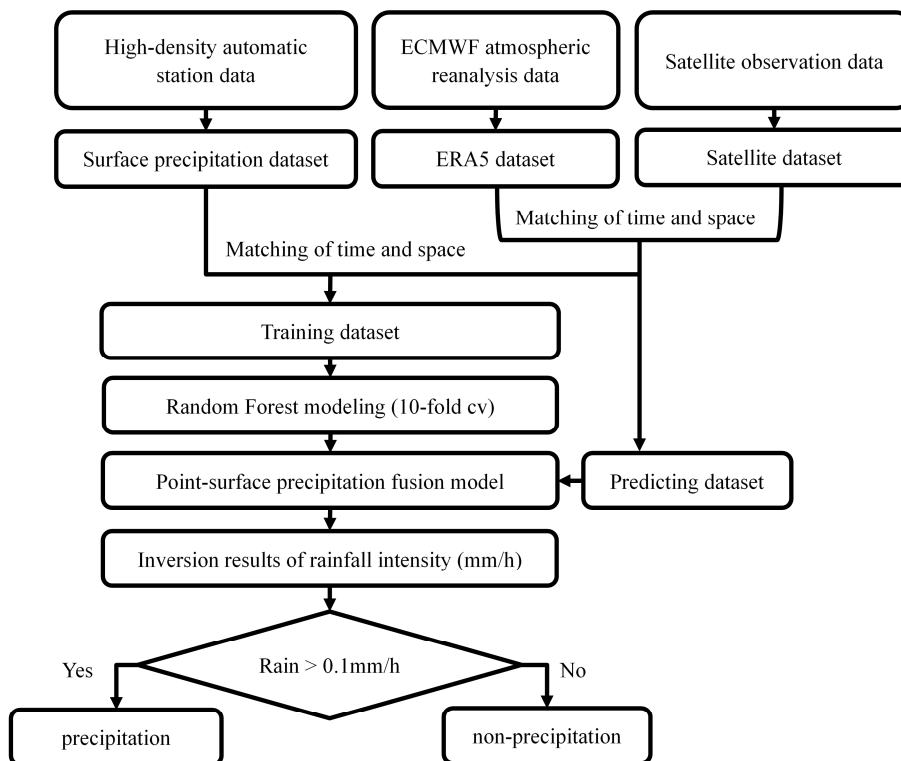


Figure 3: Flowchart for the QPE algorithm using the RF model.



580

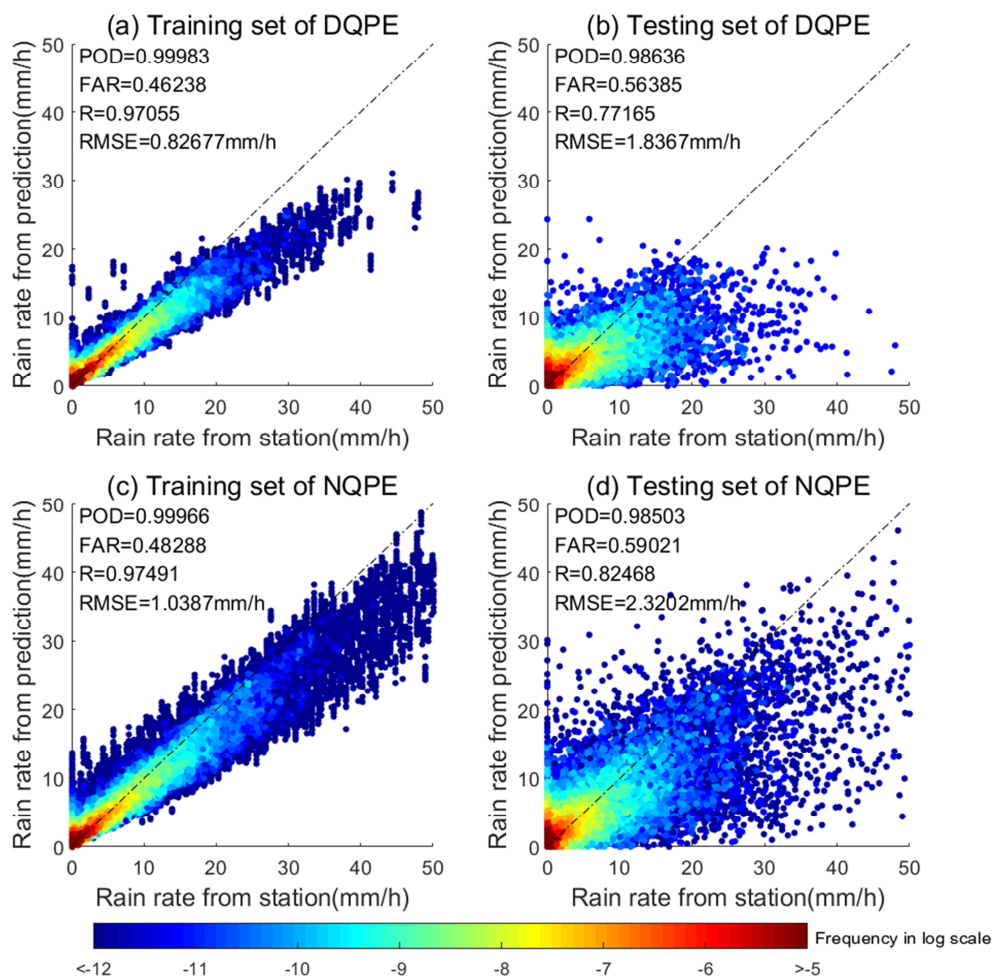


Figure 4: Comparison of the precipitation measured by high-density automatic stations and that predicted by the QPE algorithm: (a) training set of DQPE; (b) testing set of DQPE; (c) training set of NQPE; (d) testing set of NQPE. Color bar: occurrence frequency (on a log scale) at intervals of 0.5 mm/h.

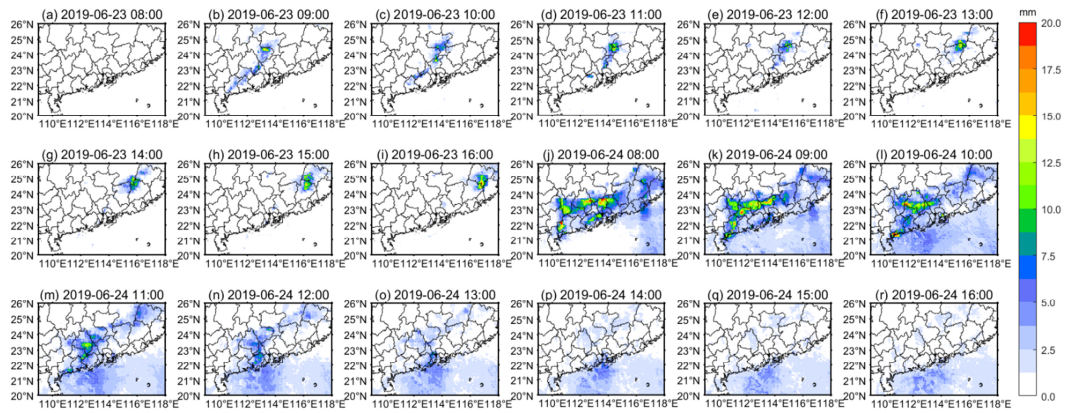


Figure 5: Predicted precipitation of the DQPE algorithm at (a–i) 0800–1600 BJT on June 23; (j–r) 0800–1600 BJT on June 24.

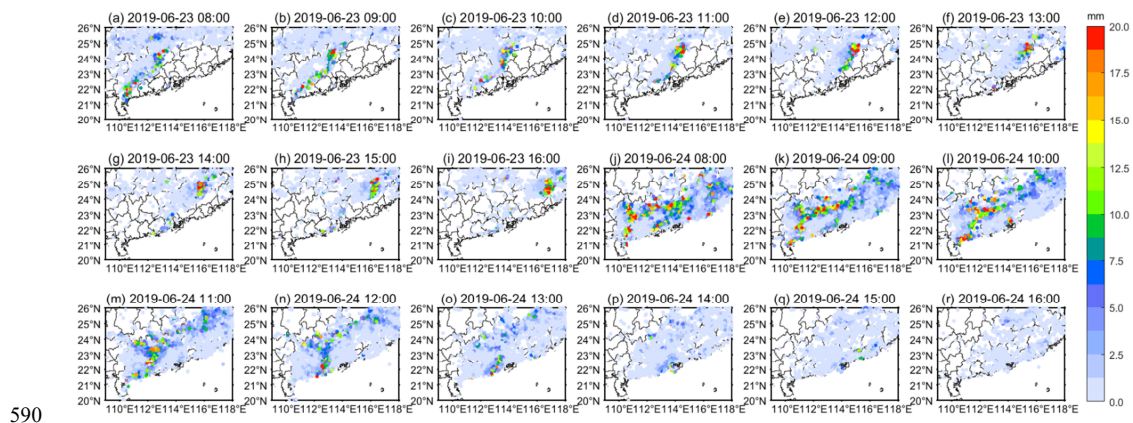
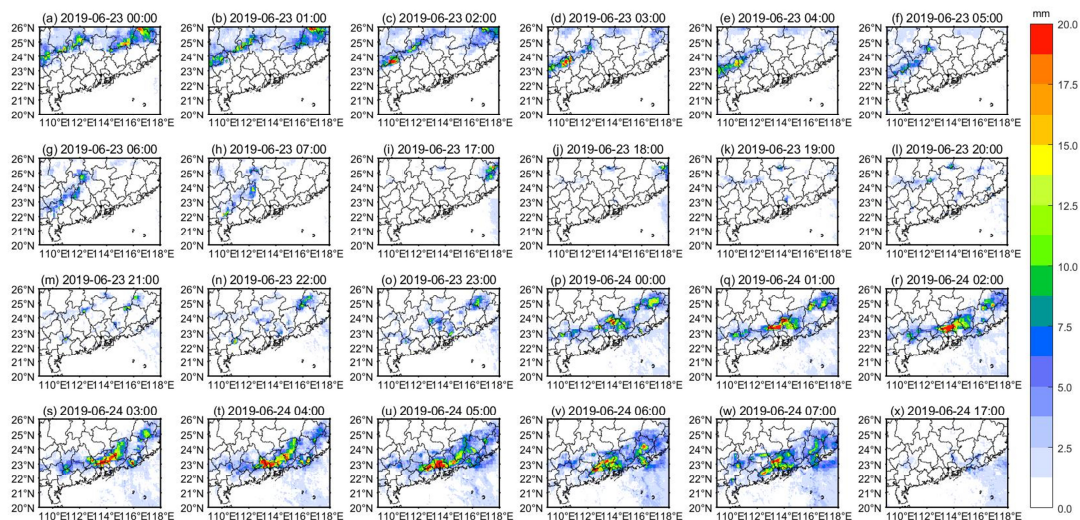


Figure 6: Actual precipitation based on high-density automatic stations at (a–i) 0800–1600 BJT on June 23; (j–r) 0800–1600 BJT on June 24.



595 **Figure 7:** Predicted precipitation of the NQPE algorithm at (a–h) 0000–0700 BJT on June 23, (i–o) 1700–2300 BJT on June 23, (p–w) 0000–0700 BJT on June 24, and (x) 1700 BJT on June 24.

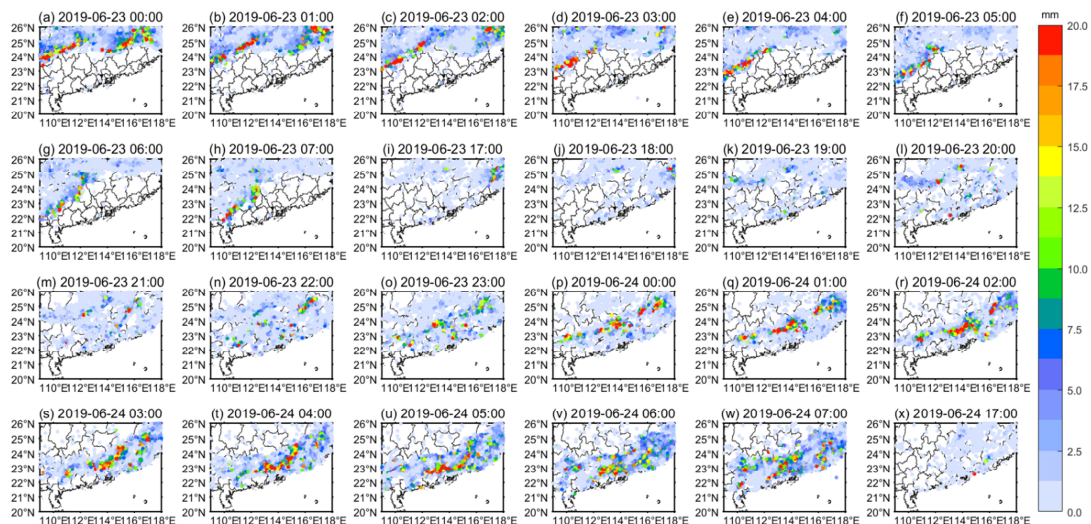


Figure 8: Actual precipitation based on high-density automatic stations at (a–h) 0000–0700 BJT on June 23, (i–o) 1700–2300 BJT on June 23, (p–w) 0000–0700 BJT on June 24, and (x) 1700 BJT on June 24.

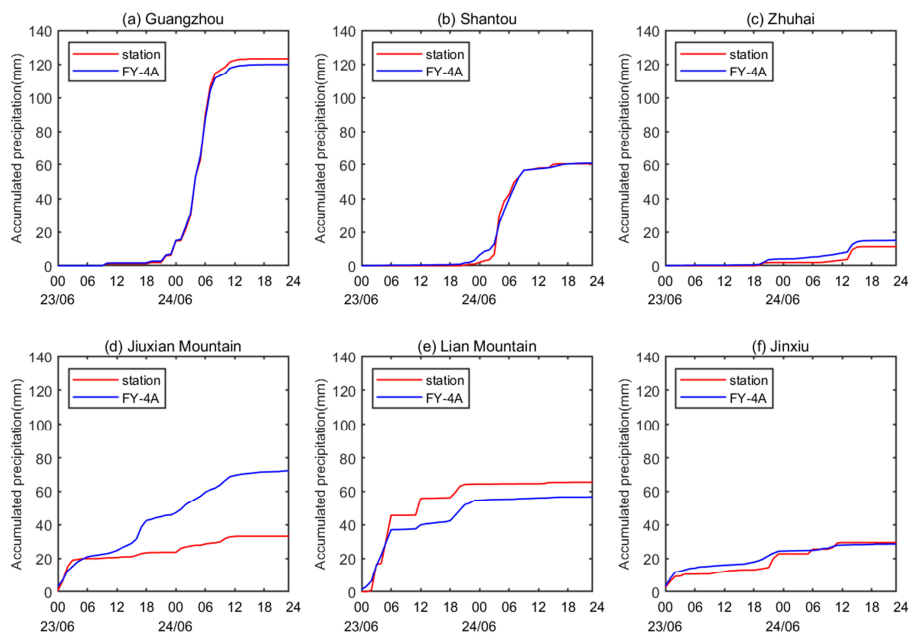


Figure 9: Accumulated precipitation in different areas: (a–c) city stations; (d–f) rural stations.

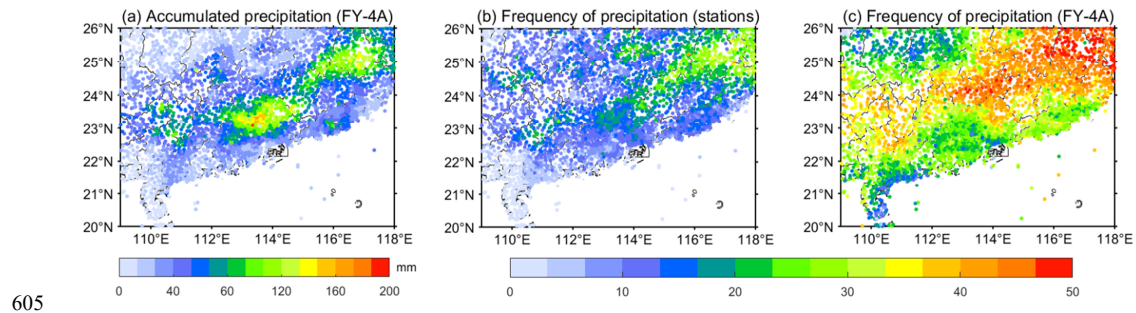
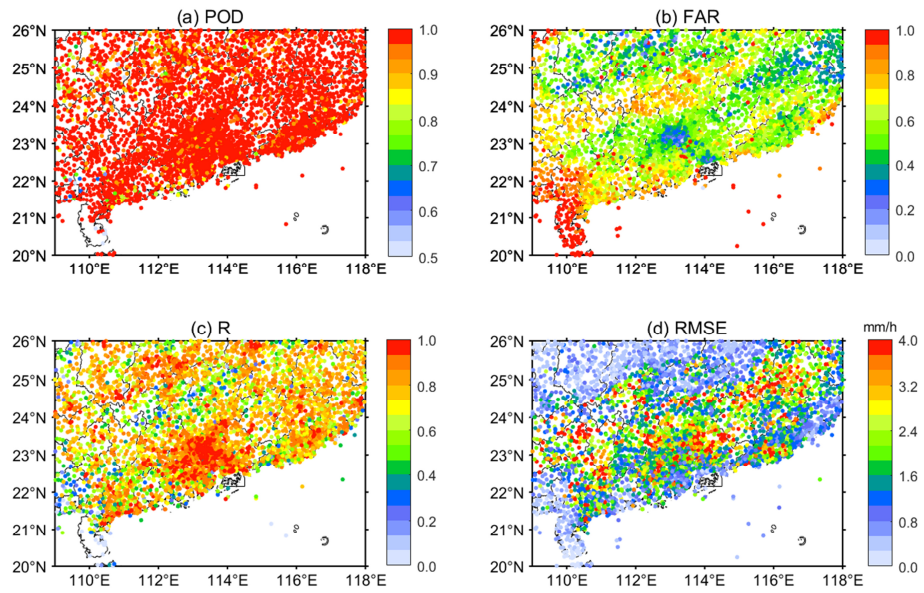
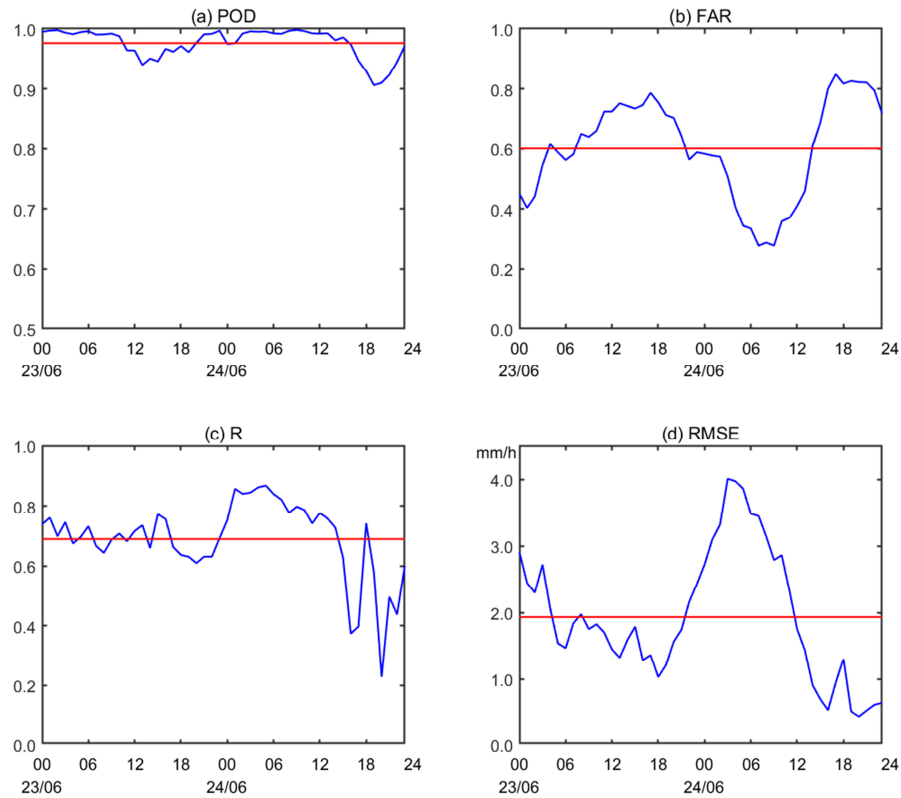


Figure 10: Spatial distribution of accumulated precipitation: (a) accumulated precipitation predicted by the QPE algorithm; (b) actual precipitation frequency observed by high-density automatic stations; (c) precipitation frequency predicted by the QPE algorithm.



610

Figure 11: Spatial distribution of evaluation indicators of the QPE algorithm for all stations: (a) POD; (b) FAR; (c) R; (d) RMSE.



615 **Figure 12:** Time series of evaluation indicators of the QPE algorithm for all stations at each time: (a) POD; (b) FAR; (c) R; (d)
RMSE.